Biosensors and Bioelectronics 141 (2019) 111468

Contents lists available at ScienceDirect

Biosensors and Bioelectronics

journal homepage: www.elsevier.com/locate/bios

Relay-race RNA/barcode gold nanoflower hybrid for wide and sensitive detection of microRNA in total patient serum

Mohsen Mohammadniaei[a], Anna Go[a], Sachin Ganpat Chavan[a], Aneesh Koyappayil[a], Seong-Eun Kim[b], Hyun Jin Yoo[a], Junhong Min[a,**], Min-Ho Lee[a,*]

[a] School of Integrative Engineering, Chung-Ang University, Heukseok-dong, Dongjak-gu, Seoul, 06910, Republic of Korea
[b] Human IT Convergence Research Center, Convergence System R&D Division, Saenari-ro, Bundang-gu, Seongnam-si, Gyeonggi-do, 13509, Republic of Korea

ARTICLE INFO

Keywords:
MicroRNA detection
Electrochemical biosensor
RNA three-way junction
Gold nanoflower platinum
Wide dynamic detection range
CHAPS

ABSTRACT

Development of a very sensitive biosensor is accompanied with an inevitable shrinkage in the linear detection range. Here, we developed an electrochemical biosensor with a novel methodology to detect microRNA-21 (miR21) at an ultralow level and broad linear detection range. A three-way junction RNA structure was designed harboring (i) a methylene blue (MB)-modified hairpin structure at its one leg to function as the sensing moiety and (ii) the other two legs to be further hybridized with barcode gold nanoparticles (MB/barG) as the signal amplifiers. Addition of target miR21 resulted in opening the hairpin moiety and subsequent hybridization with DNA-modified gold nanoflower/platinum electrode (GNF@Pt) to form the MB-3 sensor. Inspired by the relay-race run, to extend the dynamic detection range and increase the sensitivity of the biosensor, MB/barG was added to form the second detection modality (MBG-3). The combined sensor required very low sample volume (4 μL) and could identify 135 aM or 324 molecules of miR21 with the ability to operate within a wide linear range from 1 μM down to 500 aM. The fabricated GNF@Pt showed a remarkable conductivity compared with the gold nanoparticle-modified electrode. Addition of MB/barG boosted the electrochemical signal of the MB by almost 230 times. Moreover, a new protocol was introduced by the authors to increase the efficiency of microRNA extraction from the total serum. Possessing a sound selectivity and specificity towards single base-pair mutations, the developed biosensor could profile cancer development stages of two patient serums.

1. Introduction

Development of medical diagnostic devices on the basis of biomarker detection requires sensitive, cost-effective and reliable assays (Mohammadniaei et al., 2018a,b,c,d; Wu and Qu, 2015). During the last decade, microRNA (miRNA) has discovered as a very potent biomarker for the early diagnosis and treatment of several diseases (Lu et al., 2005; Mohammadniaei et al., 2018a,b,c,d; Nalejska et al., 2014). Altered expression level of this biomarker in various tissues and body fluids is associated with diverse diseases (Kato et al., 2013; Krol et al., 2010). However, short length of miRNAs (18–24 nucleotides), their highly homologous sequences and unknown abundance (ranging from aM to μM) in real samples are obstacles faced by fabrication of practical miRNA biosensors (Catuogno et al., 2011; Kilic et al., 2018; Wu and Qu, 2015). Furthermore in general, one of the important issues that imposes limits in developing any types of biosensors is the fact that increasing the sensitivity obstructs the extension of linear detection range. Therefore, introducing a new detection strategy is highly demanding to exert influence over current biosensor fabrication techniques.

Standard analytical methods such as quantitative real-time polymerase chain reaction (qRT-PCR) (Chen et al., 2011), northern blotting (NB) (Válóczi et al., 2004) and microarray-based hybridization (Li and Ruan, 2009) have been exploited for miRNA detection. For example, qRT-PCR despite its high accuracy and sensitivity, suffers from complicated primer design because of the low melting temperature of short oligonucleotides. This can cause cross-hybridization and detection errors. NB with relatively low throughput, usually demands large sample volume and requires radiolabeling causing impurities to the system. Microarray is also restricted by its complexity, cross-contamination and high cost (de Planell-Saguer and Rodicio, 2011).

Endeavors have been made to improve miRNA detection methods by implementing nanomaterials owing to their unique electrical, optical and catalytic features (Jamali et al., 2014). Various nano-based plasmonic biosensors have been developed for sensitive detection of

* Corresponding author. Tel.: +8228205503, fax.: +8228205940.
** Corresponding author.
E-mail addresses: junmin@cau.ac.kr, jmin.email@gmail.com (J. Min), mhlee7@cau.ac.kr, betbest@gmail.com (M.-H. Lee).

https://doi.org/10.1016/j.bios.2019.111468
Received 31 March 2019; Received in revised form 17 May 2019; Accepted 21 June 2019
Available online 22 June 2019
0956-5663/

miRNA, however their performances either necessitate multiple enzymes/steps or precise temperature control over the entire procedure (Driskell et al., 2008; Wang et al., 2016; Zhang et al., 2015). Likewise, signal amplification techniques have been introduced to substitute the abovementioned standard methods for precise quantification of miRNAs (Chen et al., 2018b). However, using complicated nucleic acid designs and sometimes large sample volumes make their detection systems costly and error-prone followed by poor reproducibility.

Amongst them, nano-based electrochemical biosensors have offered sensitive and cost-effective platforms for diagnostic applications (Mohammadniaei et al., 2018a,b,c,d; Mohammadniaei et al., 2018a,b,c,d; Yoon et al. 2017, 2019). For instance, three-mode electrochemical sensor represented one the most sensitive electrochemical platforms for miRNA detection (Labib et al., 2013). Though, its performance requires laborious step for p19 protein expression and purification as well as tedious washing procedures. Additionally, cleavage-mediated cascade (Zhao et al., 2013), DNA tetrahedral scaffold (Chen et al., 2018a) and hybridization chain reaction (Ge et al., 2014) methods have offered sensitive detection of miRNA down to attomolar level. However, using diverse reagents and enzymes and/or narrow linear detection range are still some shortcomings that limit their clinical applications (refer to Tables S1 and S2 for more detailed reports).

In this work inspired by the relay-race run, we developed a novel sensing mechanism comprising a two-mode supporting system (nominally MB-3 and MBG-3) to achieve a considerably low miRNA detection limit of 135 aM (324 molecules in only 4 μL of sample) in a broad linear detection range expanding from 1 μM down to 500 aM. For the sensor probe, an ultra-stable RNA three-way junction structure (3WJ) (Lee et al., 2019; Mohammadniaei et al., 2019; Shu et al., 2011) was modified harboring a methylene blue (MB)-functionalized hairpin structure (Fig. 1) and two extended barcode sequences (H-MB/Bar/3WJ). For the solid electrode, a newly-developed gold nanoflower-electrodeposited platinum structure (GNF@Pt) under a certain condition was fabricated representing a highly conductive surface. After miRNA invasion, the loop structure of the modified 3WJ was opened allowing a free over-hanged sequence to hybridize with the DNA-modified GNF@Pt following by a detectable electrochemical signal of MB. To assist the MB-3 sensor, the second mode was engaged by addition of two MB-modified barcode RNA/gold nanoparticles (MB/barG) to form the MBG-3 sensor. Interestingly, addition of MB/barG significantly amplified the MB electrochemical signal by almost 230 times to remarkably elevate the senor sensitivity and extend its detection range. Also using a simple approach by surfactant treatment of the serum, we could increase the sample recovery efficiency by ~60% which has not been reported elsewhere. The established biosensor displayed a high specificity and could successfully profile two cancer serums (breast and liver) at different development stages based on the miR21 abundance differences.

2. Results and discussion

2.1. Structure design and analysis of H-MB/Bar/3WJ in recognition of miR21

PAGE method was used to investigate the structure formation of H-MB/Bar/3WJ and its capability in selective recognition of the target miR21 (for experimental details refer to supporting information S1). The structure design was based on the 3WJ motif (black RNA sequences in Fig. 1) possessing a very stable and distinct architecture. The $3WJ_a$ strand was extended at its both ends (green sequences) as barcodes ($Bar/3WJ_a$) to be later hybridized with two MB/barG structures. The $3WJ_c$ strand was also extended at its 5′ end with a MB-modified hairpin structure ($H\text{-}MB/3WJ_c$) to arrange the final structure of H-MB/Bar/3WJ. As demonstrated in Figs. 1 and 2, the miR21 sequence is defined as two parts of *a′* and *b′* which are complementary to stem (*a*) and a portion of loop (*b*) sequences of $H\text{-}MB/3WJ_c$. After hybridization of miR21 with H-MB/Bar/3WJ, the hairpin structure of the $H\text{-}MB/3WJ_c$ is opened to form the H-MB/Bar/miR21/3WJ architecture.

As illustrated in Fig. 2 (left panel), besides the bands for the control experiment a discrete band is clearly seen at the lane 7, illustrating the successful formation of H-MB/Bar/3WJ (indicated as “Probe”). Likewise a very distinct band, higher than that of the “Probe”, can be observed at the lane 9 (indicated as “Sense”) as a result of miR21 hybridization for 1 h at RT. This shows a precise formation of the final structure H-MB/Bar/miR21/3WJ.

As it is evident in Fig. 2, the single-mismatched miR21 could poorly transform the structure where beside the intense band for “Probe”,

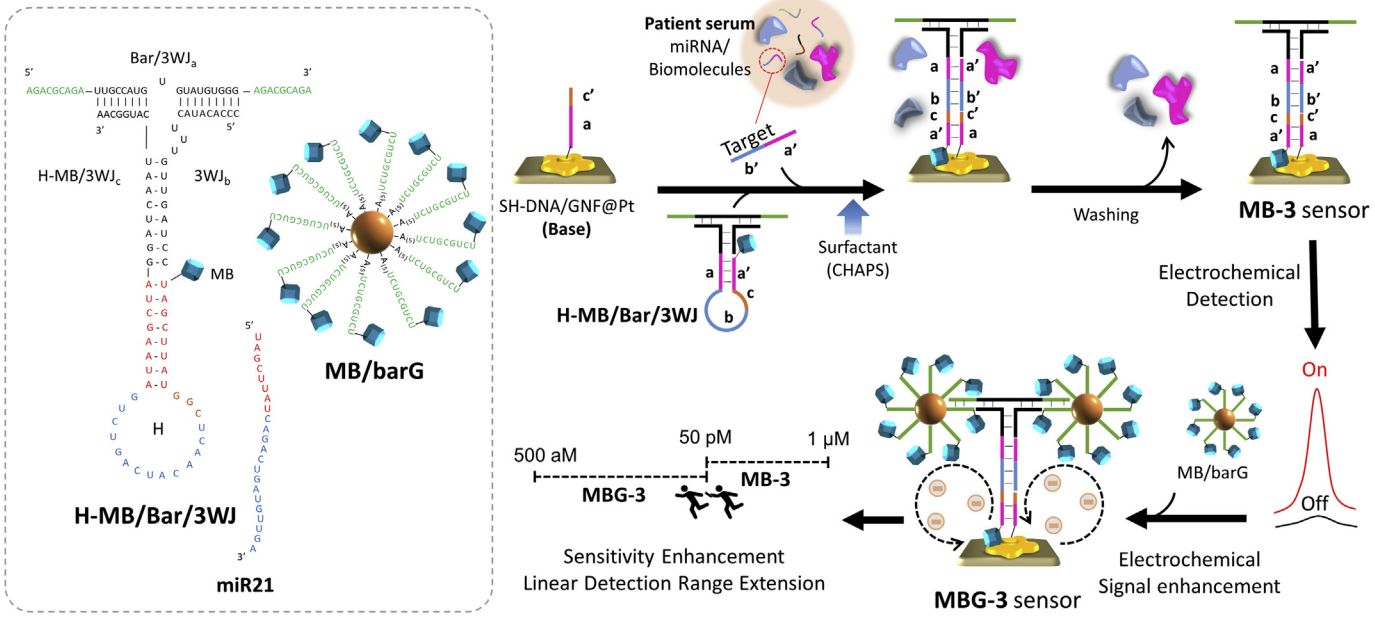

Fig. 1. Schematic diagram of the relay-race electrochemical biosensor. Left panel depicts the predicted structures and nucleic acid sequences of the H-MB/Bar/3WJ, miR21 and MB/barG.

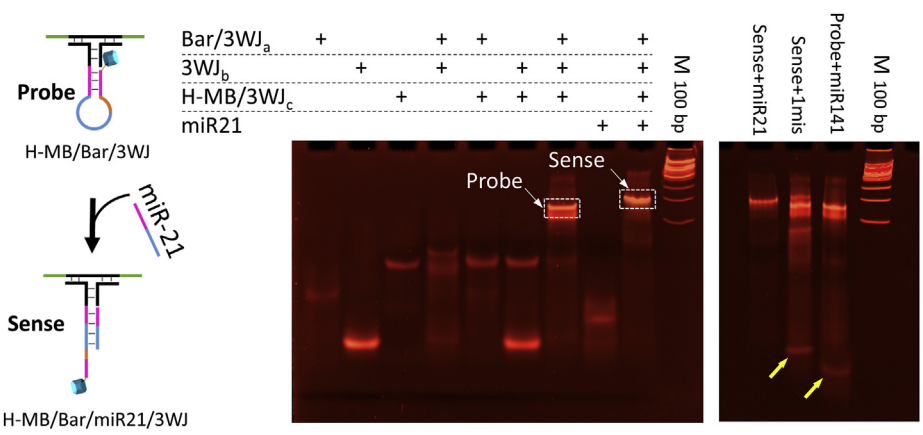

Fig. 2. Schematic diagram and native PAGE (12% TBM) results of the structure transformation from H-MB/Bar/3WJ (Probe) to H-MB/Bar/miR21/3WJ (Sense), after the addition of miR21. The ETBR staining method was used for the band visualization. Yellow arrows at the right panel illustrate the unbound miRNAs. M stands for nucleic acid marker. (For interpretation of the references to color in this figure legend, the reader is referred to the Web version of this article.)

there was a week band for "Sense". Also, majority of the miRNAs did not incorporate into the reaction (left yellow arrow). Additionally, the non-target miRNA (miR141) was incapable of structure transformation, as such, no miR141 was involved in the reaction (right yellow arrow) and no band was observed for the "Sense". The archived results confirm the robust structure of H-MB/Bar/3WJ with a high degree of selectivity and specificity.

2.2. Analysis of GNF@Pt

GNFs were selectively electrodeposited onto the platinum (Pt) electrode by reduction of $HAuCl_4$ in the presence of Tween 20 (Fig. 3a, Fig. S1 and supporting information S1). CV technique was employed and three consecutive cycles (− 0.7to 0.5 V; 50 mV/s) were recorded in the presence and the absence of Tween 20 as the structure-directing agent. Fig. 3b–f illustrate the cyclic voltammograms and the corresponding SEM images of the bare Pt electrode in 0.5 M H_2SO_4 solution as well as the gold nanostructure-modified Pt electrodes. As shown in Fig. 3b, in the presence of Tween 20, a slight negative shift (from 0.01 to 0.02 V) accompanied by a notable increase in the reduction peak of the gold (from– 2.08 to– 3.73 μA) is evident. This resulted in transfiguration of gold nanoparticle (GNP) to GNF, probably because of the role of surfactant in assisting the elongation of nanoparticles (Gao et al., 2003). Interestingly after the gold electrodeposition, reduction peak of Pt (0.21 V) was amplified by almost three times of magnitude, indicating the function of gold nanostructures as the electrochemical signal enhancers. The SEM image of GNFs (Fig. 3e) and the corresponding magnified images (Fig. 3f) clearly display the uniform and flower-like structures of GNFs on Pt electrode. Moreover, this selective electrodeposition could supply a thiol-gold bonding for the immobilization of thiolated DNAs specifically onto the working electrode.

2.3. Layer-by-layer assembly of the MB-3 and MBG-3 sensors

EIS and CV techniques were engaged to investigate the layer-by-layer formation of our biosensor (for experimental details refer to supporting information S1). Fig. 3g and h show Nyquist diagrams and the equivalent Bode plots for different modification steps of the electrode (from i to vi) in PBS (10 mM, pH 7.4) containing 5 mM $[Fe(CN)_6]^{3-/4-}$ redox probe and 0.1 M KCl. The R_{ct} of Pt electrode was 875.6 Ω and further decreased by 84% to 135.2 Ω after formation of GNP@Pt, suggesting a higher charge transfer efficiency at the electrode/electrolyte interface. However, a very negligible value of 5.32 Ω was observed for the GNF@Pt. This illustrates a pronounce electron conductivity of the modified electrode, resulting from the higher surface-to-volume ratio of GNF compared to GNP together with a synergistic effect of the flower-like gold nanostructures and the Pt. Also from the Bode plots in Fig. 3h, almost no peak at the mid frequency region (corresponds to charge transfer resistance) was observed for GNF@Pt, indicating its negligible $|Z|$ value.

After immobilization of thiolated DNA on the GNF@Pt and further electrode backfilling by 6-Mercapto-1-hexanol (MCH) (formation of *Base* structure), there was a pronounce increase in the R_{ct} value to 1628.4 Ω. This may have occurred because of the blockage as well as electrostatic repulsion of the redox probe ($Fe(CN)_6^{3-4-}$) *via* the negatively charged DNA and MCH immobilized onto the GNF@Pt. Hybridization of H-MB/Bar/miR21/3WJ with *Base* further resulted in an increase in the R_{ct} value to 1813.1 Ω, suggesting the successful formation of MB-3 sensor. Moreover, hybridization of GNP[10]-modified MB/Bar (MB/BarG) with the structure (formation of MBG-3 sensor) was followed by subsequent increment of R_{ct} to 2530.6 Ω. Characterization of MB/BarG is provided in supporting information S2 and Fig. S2. This may be attributed to the imposition of a considerable negative charge (MB/barG) and an extra resistance (blockage of the redox probe) to the surface to damp the charge transfer rate between the electrode and the solution. Similar results can be observed from the Bode diagrams (Fig. 3h), as there was a sequential increase of $|Z|$ value after each step of immobilization.

In addition, CV technique was used to better perceive the structure formation of MB-3 and MBG-3 sensors. As depicted in Fig. 3i and Fig. S3, comparing to the voltammograms recorded for GNF@Pt and the *Base*, a clear quasi-reversible redox signal for MB-3 was seen at– 0.37 V and– 0.28 V, arising from the MB. For 50 pM miR21, the reduction and oxidation current peaks of the MB-3 sensor were + 0.046 ± 0.007 and –0.059 ± 0.012 μA, respectively. Whereas, those values for the MBG-3 sensor (50 pM miR21) were measured + 10.37 ± 0.32 and – 13.21 ± 0.53 μA, respectively. Accordingly, the MBG-3 redox current signals were almost 230 times higher than those of the MB-3 signals, suggesting a considerable function of the MB/barG on the electrochemical signal amplification of MB. This can be ascribed to a dual effect of (first) elevating the number of MB molecules and (second) the role of gold nanoparticles as the well-known electrochemical signal enhancers. The obtain data confirm the layer-by-layer self-assembly of the MB-3 and MBG-3 sensors.

2.4. Sensor performance

The sensor performance was based on the detection of electrochemical signal arising from MB as a result of target hybridization. DPV technique was employed and the oxidation current peak of the MB was chosen as the detection signal. The *Base* structure was formed by immobilization of thiolated DNA on the GNF@Pt (for experimental details refer to supporting information S1). The detection probe was composed of the *Base* and an excess amount of H-MB/Bar/3WJ. As seen in Fig. 1, the designed H-MB/Bar/3WJ consisted of a core 3WJ structure ($3WJ_a$, $3WJ_b$ and $3WJ_c$) which was modified at its three legs. The $3WJ_a$ was extended at its both ends by homologous sequences (green color) complementary to the RNA sequences of the MB/barG. The $3WJ_c$ was

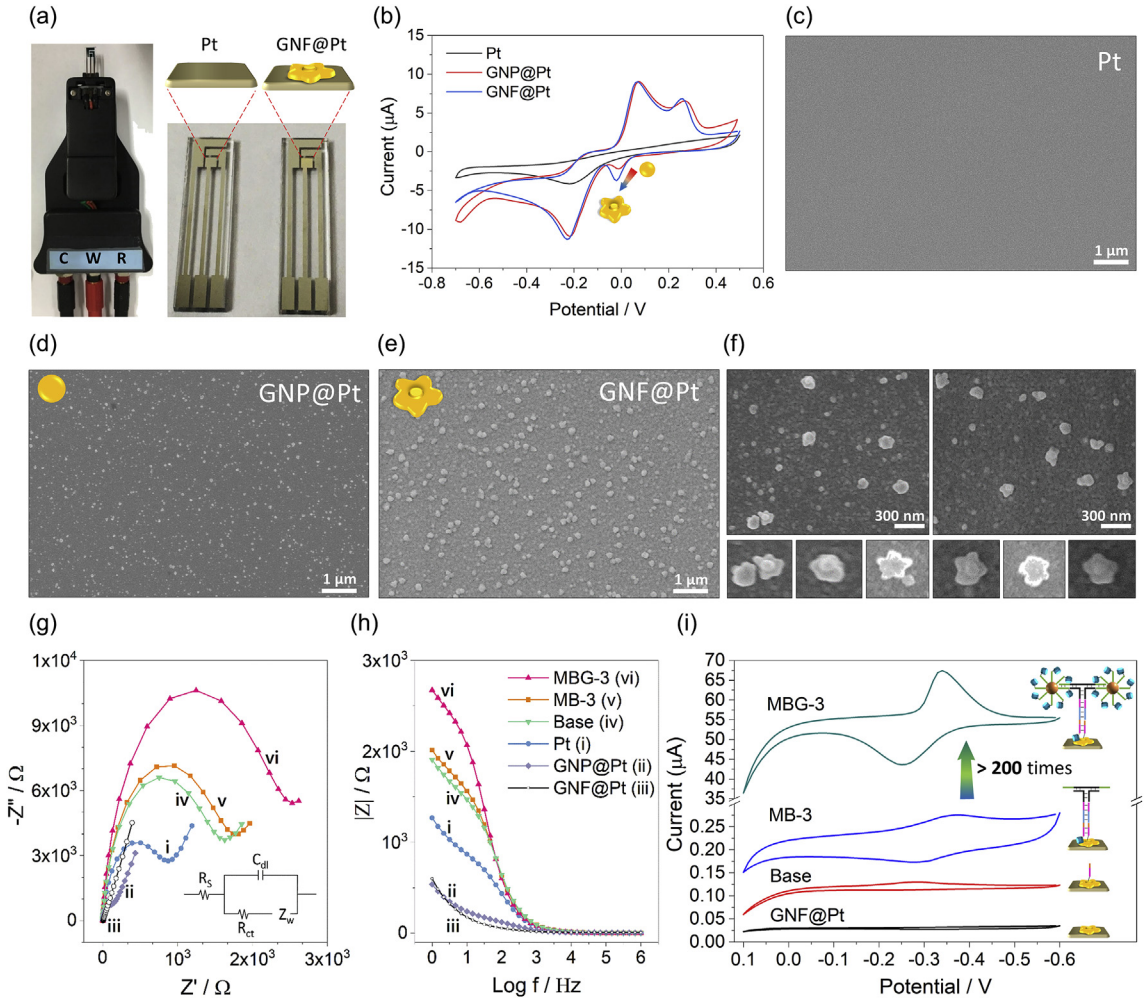

Fig. 3. a) Optical images of the platinum electrode configuration fabricated on the slide-glass substrate, before and after the GNF electrodeposition; Yellow color of the working electrode can be clearly seen after the GNF electrodeposition. b) Cyclic voltammograms of the 3rd cycles for different modification of Pt electrode; Scan rate: 50 mV/s c-e) SEM images from the Pt electrode surfaces before and after gold electrodeposition. f) Magnified SEM images of the GNF@Pt. g and h) Nyquist plots (Z′ vs.−Z″) and the equivalent bode plots obtained for (i) bare Pt, (ii) GNP@Pt, (iii) GNF@Pt, (iv) DNA-modified GNF@Pt (*Base*), (v) MB-3 sensor and (vi) MBG-3 sensor; The inset in Fig. 3g demonstrates the equivalent Randles circuit model; All the experiments were carried out in PBS buffer (pH 7.4) containing 5 mM $Fe(CN)_6^{4-/3-}$ and 0.1 M KCl. i) Comparison between the cyclic voltammograms recorded for GNF@Pt, *Base*, MB-3 and MBG-3 structures.

also extended at its 5′ end to a MB-modified hairpin structure (H) whose stem and the long portion of its loop (denoted as: *a* and *b*) were complementary to the target miR21 sequence (defined as two sequence parts of *a′* and *b′*). Besides, the DNA sequence of the *Base* (*a* and *c′*) was partially complementary to the H motif at its stem (*a′*) and a short portion of its loop (*c*). In the absence of the target miRNA (miR21) and also in the presence of non-target strands, the H structure remained intact. Addition of target miRNA resulted in hybridization of *b′* with *b* and further *a′* with *a* to open the loop of H-MB/Bar/3WJ, because the hybrid form (H-MB/Bar/miR21/3WJ) has more base pairs than that of the stem in the H motif (H-MB/Bar/3WJ) and is therefore more stable. Then, the sequences of a' and c were discharged to become available for hybridization with DNA at the *Base*. This was followed by attachment of the MB to the GNF@Pt and a detectable electrochemical signal arising from MB (formation of MB-3 sensor).

Higher concentration of miR21 was followed by increasing the number of H-MB/Bar/miR21/3WJ on the *Base.* This contributed to the attachment of more MB molecules on the surface leading to a higher redox current signal of MB. As shown in Fig. 4a, increment of miR21 concentration led to increasing the oxidation current of MB. The developed MB-3 sensor could cover a linear detection range from 1 μM to 50 pM (Fig. 4b).

To further enhance the detection range of the system where the MB-3 sensor was incapable of working, MB/BarG was added to hybridize with the extended barcode sequences at $Bar/3WJ_a$ strand and form the MBG-3 sensor. As demonstrated in Fig. 4c and d and previously described in section 2.3, a synergic effect resulted in boosting the electrochemical signal of MB and gave rise to the extension of linear detection range down to 500 aM. As illustrated in Fig. 4b and d, working ranges of MB-3 and MBG-3 sensors are defined within the linear regions where beyond those ranges sensors were either saturated or unable to detect the target. The fabricated sensor with a broad linear detection range (1 μM–500 aM) required only 4 μL of the sample volume which remarkably reduces the detection costs. The limit of detection (LOD) was calculated 135 a.m. (324 molecules in 4 μL) on the basis on the $3 \times (S_b/A)$ method, where A is the slope of the linear fitting curve and S_b is the standard deviation of the blank signal. The optimal detection time for MB-3 and MBG-3 sensors were chosen 80 min and 130 min, respectively (Supporting information S3 and Fig. S4).

Selectivity test was also performed using different miRNAs (single-mismatched miR21, miR152, miR155 and miR141). As it is evident in Fig. 5a and its inset, the signal detected for single-mismatched miR21 (1 M-miR21) was around 57% lower than that of the miR21, whereas for the non-target miRNAs almost no signals were detected. These results which are in consistence with the PAGE analysis data, demonstrate a high degree of specificity and selectivity of the developed biosensor.

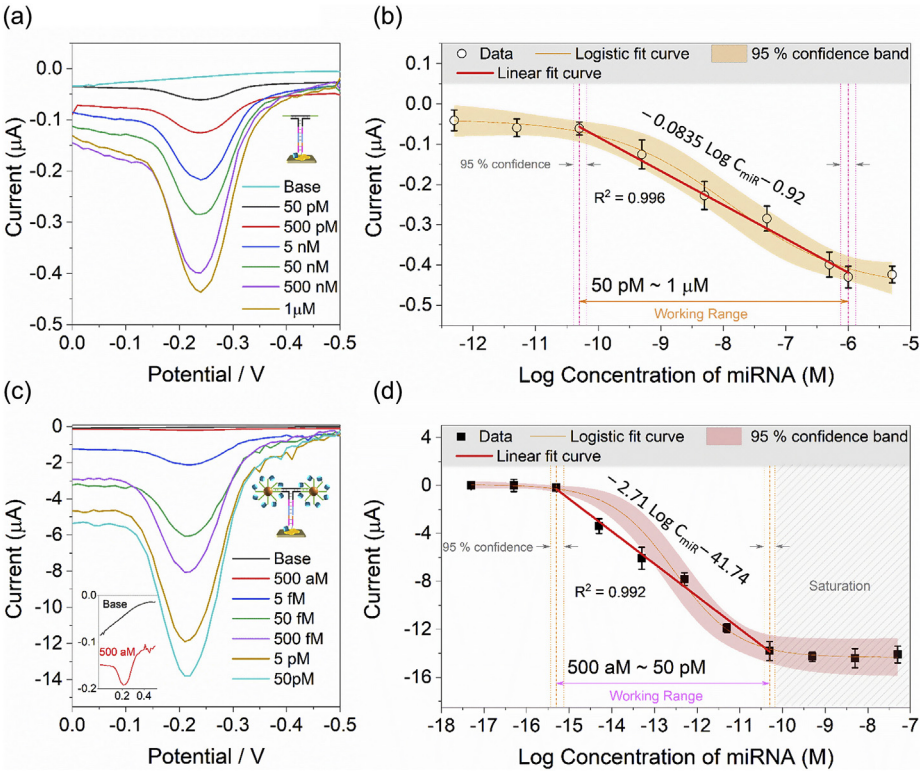

Fig. 4. a) Differential pulse voltammograms recorded before and after exposure of the MB-3 sensor with various concentrations of miR21. b) Changes in reduction current of the MB after formation of MB-3 sensor by addition of different concentrations of miR21 from 0.5 pM to 5 μM; The linear range (working range) was observed from 50 pM to 1 μM. c) Differential pulse voltammograms obtained from MBG-3 sensor with different amounts of miR21; Inset shows the magnified curves of the Base and 500 aM miR21. d) Changes in reduction current of the MB after formation of MBG-3 sensor by addition of different concentrations of miR21 from 5 aM to 50 nM; The working range was observed from 500 aM to 50 pM. Statistical data was obtained from eight different samples under identical conditions and 95% confidence was considered.

Furthermore, performance of the developed biosensor was compared with the qRT-PCR. As shown in Fig. 5b, considering the C_t value, the qRT-PCR represented a linear detection range from 500 nM to 5 fM with a good selectivity and a LOD of 1.23 fM. Given the observed data, out developed biosensor displayed a higher sensitivity and a broader linear detection range without using any enzyme and the step for the reverse transcription, to be further employed as a promising system for miRNA detection.

For the stability test, cyclic voltammograms of the sensors were monitored for 100 cycles (Fig. 6a and b) and 200 cycles (Fig. S5). As it

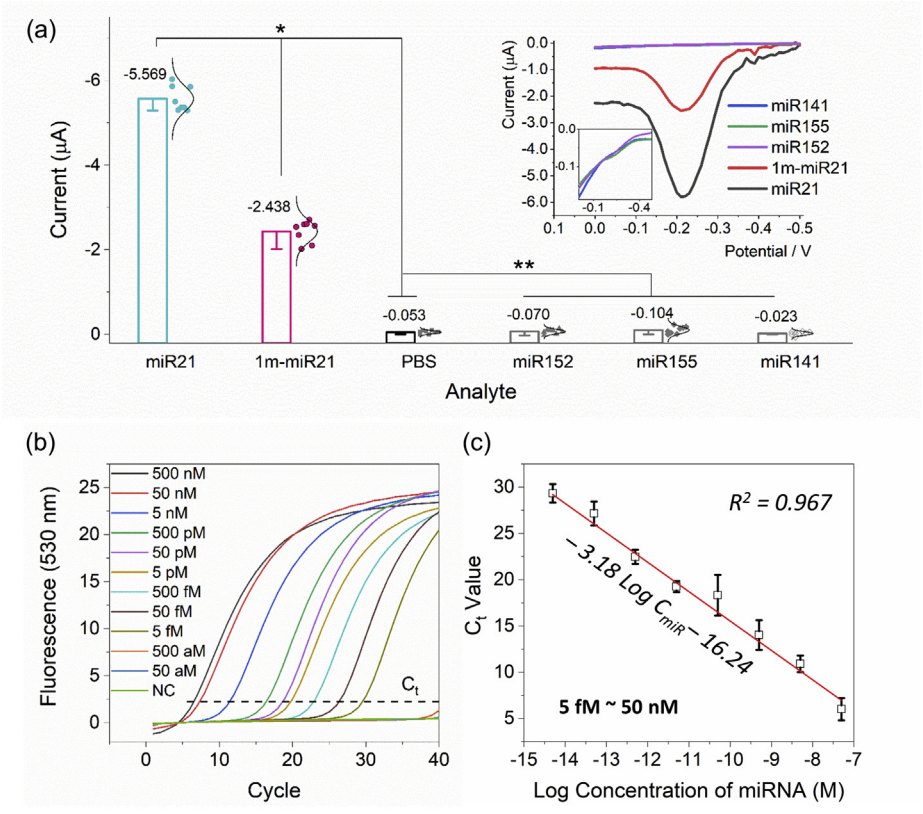

Fig. 5. a) Selectivity of the MBG-3 sensor for the detection of 50 fM miR21in the mixture of miRNAs, single-mismatched miR21 (1m-miR21) and 500 fM non-target miRN0As (miR-152, miR-155 and miR-141) as the comparison with the control PBS; Inset-1 shows typical corresponding differential pulse voltammograms; Inset-2 displays the magnified curves for miR152, miR155 and miR141; Error bars were calculated based on the recorded data from 8 identical samples; $*P < 0.05$ and $**P < 0.03$ vs. control. b) qRT-PCR experiment for the TaqMan fluorescence monitoring of the amplification reactions triggered by various concentrations of miR21; dash line displays the C_t value. c) Corresponding plot of the C_t value as a function of miR21 concentration; Data analysis was carried out using LightCycler® Software 4.05 (Roche Applied Science). For the qRT-PCR, the error bar was calculated based on 3 identical samples.

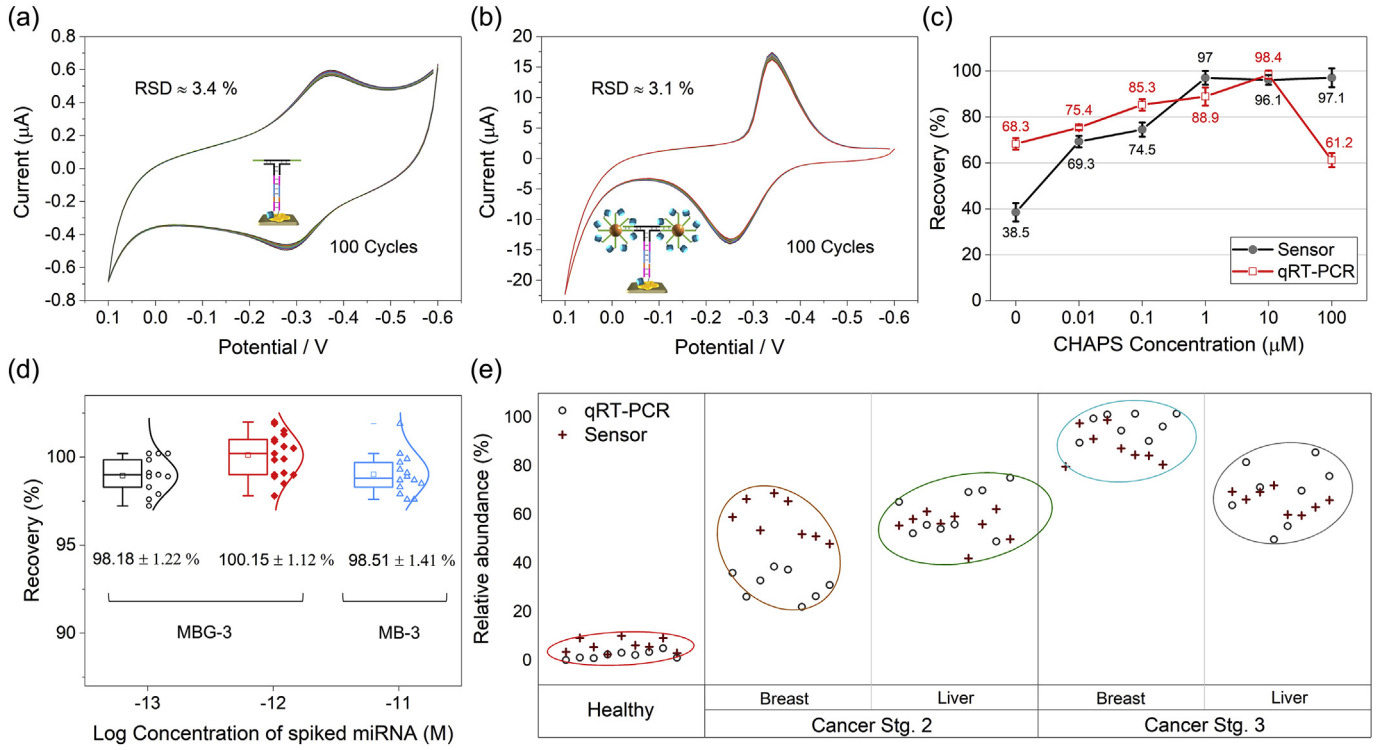

Fig. 6. a and b) Stability analysis of MB-3 and MBG-3 sensors confirmed by running 100 cycles of CV; Each 10 cycles are shown. c) Sample recovery from spike-in serum as a function of CHAPS concentration; 1 pM of synthetic miR21 was spiked into 10% HSA. d) Sample recovery from HSA treated with 10 μM CHAPS and different concentrations of spiked synthetic miR21; Data obtained from at least eight different experiments and error bars were calculated based on the standard deviations of the mean value. e) Statistical data of the relative abundance of miR21 inside the healthy and cancerous (breast and liver) serums at two development stages (2 and 3) obtain from qRT-PCR and the developed sensor; At least eight data was recorded for each method and 95% of confidence was considered for the ellipse curves.

is evident, after 100 cycles MB-3 and MBG-3 sensors represented competent stability with relative standard deviation (RSD) of 3.4% and 3.1%, respectively. Also after 200 cycles, both sensor modalities represented sound stabilities.

In addition, repeatability test for both MB-3 and MBG-3 sensors were carried out. As seen in Fig. S6, two sets of sensors (8 sensors each) were prepared under identical conditions and directed to the DPV analysis. After the measurement, all of the samples were washed, dried and kept in a proper humid chamber for further experiments. The measurement was repeated on all of the samples over 12 h with the interval of 2 h. A very slight change in the detected signal was observed for both sensors (RSD for MB-3 = 1.9% and for MBG-3 = 2.04%), illustrating their sound repeatability (Fig. S7). Moreover, MB-3 and MBG-3 sensors demonstrated sound reproducibility as they could respectively retain 96.8% and 98.2% of their initial signal values after being stored for 4 weeks at 4 °C in a humid chamber.

2.5. Real sample analysis

2.5.1. Function of CHAPS on the miRNA recovery from serum

Prior to the final experiment, we investigated the role of CHAPS on the miRNA recovery from serum. As reported earlier, CHAPS can effectively eliminate protein aggregations (Lee et al., 2010). Therefore we speculated that, CHAPS would facilitate the release of the exogenous nucleic acids buried inside the microparticles composed of various proteins/peptides/biomolecules in serum. 1 pM of synthetic miR21 was spiked into 10% HSA and treated with different concentrations of CHAPS (0.01–100 μM) in the presence of an excess amount of yeast tRNA (for experimental details refer to supporting information S1). After incubation, samples were tested using qRT-PCR and MBG-3 sensor. As it is evident in Fig. 6c, addition of CHAPS had a big impact on the sample recovery where its optimum concentration was found 10 μM for both qRT-PCR and MBG-3 sensor. Increasing the concentration of CHAPS from 0 to 1 μM resulted in gradual increment in sample recovery of the MBG-3 sensor from ~38.5% to ~97%. Addition of more amount of CHAPS did not have a notable impact on the sensor performance. Likewise, a similar trend was observed from the qRT-PCR experiment where the sample recovery slightly increased from ~68.3% to ~98.4% by 10 μM of CHAPS before a drop to ~61.2% upon increasing its concentration to 100 μM. As confirmed by both methods, despite the clear impact of CHAPS on the miRNA recovery from the serum, CHAPS showed more effect on the MBG-3 sensor than that of the qRT-PCR. This may result from its probable interference with different reagents and enzymes used in qRT-PCR to hamper their effective performances. As a result, we used 10 μM of CHAPS in the further experiments. Different concentration of miR21 was spiked into the 10% human serum and directed to the measurement by MB-3 and MBG-3 sensors. The sample recovery was calculated on the basis of standard addition method. As depicted in Fig. 6d, a sound recovery of 98.18%–100.15% was observed indicating that the fabricated biosensor has a considerable potential to work in real biological environments.

A side-by-side comparison experiment was also performed using our technique and qRT-PCR for the detection of different concentrations of miR21 spiked in 10% serum treated with 10 μM CHAPS. As illustrated in Fig. S8, similar performance was observed, however our sensor represented wider linear detection range from 5 fM to 1 μM compared to the qRT-PCR (50 fM to 50 nM). This might be due to the possible interference of the serum proteins with the enzymes used in the reverse transcription and amplification steps of qRT-PCR. Also the percentage of slope deviation between the linear curves in 10% serum (Fig. S8c) and in PBS (Fig. 4b and d) was 7.1% and 5.5% for MB-3 and MBG-3 sensors, respectively, proving a very low non-specific interference on the developed sensor. As the control experiment, we also performed similar tests on the 10% serum without CHAPS treatment (Fig. S9) and

the slop deviation increased up to 66% and 57% with narrower dynamic range for MB-3 and MBG-3 sensors, respectively, to demonstrate the capability of our sensor to operate in real biological matrices.

Moreover the biofouling effect on the sensor was investigated using EIS technique. As seen in Fig. S10, the measured R_{ct} for the MB-3 and MBG-3 sensors in PBS was 1840.41 and 2586.44 Ω, respectively. However, these values were a bit higher (12.1% and 15.3%) when measuring in 10% serum (with 10 μM CHAPS treatment), illustrating protein adsorption on the electrode surface to hamper the electron transfer rate between the solution and electrode. Although, fortunately the issue did not have a considerable impact on the measured DPV signal, as studied above. In addition, in case of the measurement without CHAPS treatment, the R_{ct} for the MB-3 and MBG-3 sensors was substantially higher (75.3% and 83.3%, respectively), illustrating the function of CHAPS on reducing the non-specific adsorptions to be a thought-provoking strategy for many research disciplines.

2.5.2. Profiling of miR21 in total patient serum

We employed the developed sensor to detect endogenous circulating has-miR21 in total human serums obtained from healthy and cancerous (breast and liver cancers; stage 2 and 3) donors (Table S4). Total circulating nucleic acid was purified from pure serums using QIAamp® Circulating Nucleic Acid kit with some modifications of CHAPS and tRNA treatment (for experimental details refer to supporting information S1). As demonstrated in the normalized statistical data of Fig. 6e, compared with the healthy samples the cancerous ones contained higher miR21 level. In addition, the miR21 abundance of stage 3 for both cancerous samples was higher than that of the stage 2. However, in breast cancer stage 3 it was ~44% higher than the stage 2. Also, in case of the liver cancer samples, the difference was not that much considerable (~8%). Observing the notable difference between the miR21 abundance in breast cancer stage 2 and 3 would be an interesting topic to be considered for the early diagnosis of different development stages of various cancers. The obtained results was in consistence with the qRT-PCR data, illustrating that our method is highly reliable and well-capable of miRNA detection in clinical samples. Importantly, the difference between the measured miR21 level by our method and qRT-PCR could be ascribed to the post-treatment of the purified nucleic acids with different enzymes and reagents during the reverse transcription and amplification steps for the qRT-PCR.

3. Conclusion

A newly-developed enzyme-free electrochemical miRNA detection mechanism was reported to enhance the sensitivity (down to 135 aM) and to widen the dynamic range of the biosensor from 1 μM to 500 aM using two modalities of MB-3 and MBG-3 in a relay-race supporting situation. The MBG-3 sensor represented almost 230 times higher electrochemical signal than that of the MB-3 sensor to give rise to the sensitivity and detection range enhancement of the biosensor. The amplified signal could be attributed to the elevated numbers of MBs on the solid surface as well as the role of gold nanoparticles in facilitating the electron tunneling through the nanocomplex. Moreover, electrodeposition of Pt with GNF generated a significant electron conductive nanostructure with a high surface to volume ratio to accelerate the electron transfer rate between the electrode and MB. The fabricated biosensor displayed a remarkable capability of miR21 detection in total patient serum. In addition, treatment with an optimum concentration of CHAPS (10 μM) was found to increase the recovery efficiency of miRNA from serum, to open a new horizon for the production of clinical diagnostic devices. The proposed relay-race strategy could be generalized for the development of any types of biosensors with aim of addressing the dynamic detection range restrictions.

Conflict of interest

Authors declare no conflict of interest.

Declaration of interests

The authors declare that they have no known competing financial interests or personal relationships that could have appeared to influence the work reported in this paper.

CRediT authorship contribution statement

Mohsen Mohammadniaei: Methodology, Validation, Visualization, Formal analysis, Writing - review & editing. **Anna Go:** Resources, Software. **Sachin Ganpat Chavan:** Writing - review & editing. **Aneesh Koyappayil:** Methodology. **Seong-Eun Kim:** Writing - original draft. **Hyun Jin Yoo:** Resources. **Junhong Min:** Conceptualization, Supervision. **Min-Ho Lee:** Funding acquisition, Project administration, Supervision, Writing - review & editing.

Acknowledgment

This work is supported by the Ministry of Trade, Industry, and Energy (Grant no. P0005440 and Grant no. 20000580).

Appendix A. Supplementary data

Supplementary data to this article can be found online at https://doi.org/10.1016/j.bios.2019.111468.

References

Catuogno, S., Esposito, C.L., Quintavalle, C., Cerchia, L., Condorelli, G., De Franciscis, V., 2011. Cancers 3, 1877–1898.
Chen, C., Tan, R., Wong, L., Fekete, R., Halsey, J., 2011. Quantitation of MicroRNAs by real-time RT-qPCR. In: Park, D.J. (Ed.), PCR Protocols. Humana Press, Totowa, NJ, pp. 113–134.
Chen, Y.-X., Huang, K.-J., He, L.-L., Wang, Y.-H., 2018a. Biosens. Bioelectron. 100, 274–281.
Chen, Y.-X., Huang, K.-J., Niu, K.-X., 2018b. Biosens. Bioelectron. 99, 612–624.
de Planell-Saguer, M., Rodicio, M.C., 2011. Anal. Chim. Acta 699, 134–152.
Driskell, J.D., Seto, A.G., Jones, L.P., Jokela, S., Dluhy, R.A., Zhao, Y.P., Tripp, R.A., 2008. Biosens. Bioelectron. 24, 917–922.
Gao, J., Bender, C.M., Murphy, C.J., 2003. Langmuir 19, 9065–9070.
Ge, Z., Lin, M., Wang, P., Pei, H., Yan, J., Shi, J., Huang, Q., He, D., Fan, C., Zuo, X., 2014. Anal. Chem. 86, 2124–2130.
Jamali, A.A., Pourhassan-Moghaddam, M., Dolatabadi, J.E.N., Omidi, Y., 2014. TrAC Trends Anal. Chem. (Reference Ed.) 55, 24–42.
Kato, M., Castro, N.E., Natarajan, R., 2013. Free Radical Biol. Med. 64, 85–94.
Kilic, T., Erdem, A., Ozsoz, M., Carrara, S., 2018. Biosens. Bioelectron. 99, 525–546.
Krol, J., Loedige, I., Filipowicz, W., 2010. Nat. Rev. Genet. 11 (9), 597–610.
Labib, M., Khan, N., Ghobadloo, S.M., Cheng, J., Pezacki, J.P., Berezovski, M.V., 2013. J. Am. Chem. Soc. 135, 3027–3038.
Lee, T., Ahmed El-Said, W., Min, J., Oh, B.-K., Choi, J.-W., 2010. Ultramicroscopy 110, 712–717.
Lee, T., Park, S.Y., Jang, H., Kim, G.-H., Lee, Y., Park, C., Mohammadniaei, M., Lee, M.-H., Min, J., 2019. Mater. Sci. Eng. C 99, 511–519.
Li, W., Ruan, K., 2009. Anal. Bioanal. Chem. 394, 1117–1124.
Lu, J., Getz, G., Miska, E.A., Alvarez-Saavedra, E., Lamb, J., Peck, D., Sweet-Cordero, A., Ebert, B.L., Mak, R.H., Ferrando, A.A., Downing, J.R., Jacks, T., Horvitz, H.R., Golub, T.R., 2005. Nature 435, 834–838.
Mohammadniaei, M., Lee, T., Bharate, B.G., Yoon, J., Choi, H.K., Park, S.-j., Kim, J., Kim, J., Choi, J.-W., 2018a. Small 14, 1802934.
Mohammadniaei, M., Park, C., Min, J., Sohn, H., Lee, T., 2018b. Fabrication of electrochemical-based bioelectronic device and biosensor composed of biomaterial-nanomaterial hybrid. In: Noh, I. (Ed.), Biomimetic Medical Materials: from Nanotechnology to 3D Bioprinting. Springer Singapore, Singapore, pp. 263–296.
Mohammadniaei, M., Yoon, J., Choi, H.K., Placide, V., Bharate, B.G., Lee, T., Choi, J.-W., 2019. ACS Appl. Mater. Interfaces 11, 8779–8788.
Mohammadniaei, M., Yoon, J., Lee, T., Bharate, B.G., Jo, J., Lee, D., Choi, J.-W., 2018c. Small 14, 1703970.
Mohammadniaei, M., Yoon, J., Lee, T., Choi, J.-W., 2018d. J. Biotechnol. 274, 40–46.
Nalejska, E., Mączyńska, E., Lewandowska, M.A., 2014. Mol. Diagn. Ther. 18, 273–284.
Shu, D., Shu, Y., Haque, F., Abdelmawla, S., Guo, P., 2011. Nat. Nanotechnol. 6, 658–667.
Válóczi, A., Hornyik, C., Varga, N., Burgyán, J., Kauppinen, S., Havelda, Z., 2004. Nucleic Acids Res. 32 e175-e175.

Wang, H.-N., Crawford, B.M., Fales, A.M., Bowie, M.L., Seewaldt, V.L., Vo-Dinh, T., 2016. J. Phys. Chem. C 120, 21047–21055.
Wu, L., Qu, X., 2015. Chem. Soc. Rev. 44, 2963–2997.
Yoon, J., Mohammadniaei, M., Choi, H.K., Shin, M., Bapurao G, B., Lee, T., Choi, J.-W., 2019. Appl. Surf. Sci. 478, 134–141.
Yoon, J., Shin, J.-W., Lim, J., Mohammadniaei, M., Bharate Bapurao, G., Lee, T., Choi, J.-W., 2017. Colloids Surf., B 159, 729–736.
Zhang, H., Liu, Y., Gao, J., Zhen, J., 2015. Chem. Commun. 51, 16836–16839.
Zhao, Y., Zhou, L., Tang, Z., 2013. Nat. Commun. 4, 1493.